



The Milky Way Bulge Extra-tidal Star Survey: BH 261 (AL 3)

Andrea Kunder¹ , Zdenek Prudil² , Kevin R. Covey³ , Joanne Hughes⁴ , Meridith Joyce^{5,6} , Iulia T. Simion⁷ ,
Rebekah Kuss^{1,8}, Carlos Campos¹ , Christian I. Johnson⁹ , Catherine A. Pilachowski¹⁰ , Kristen A. Larson³,
Andreas J. Koch-Hansen¹¹ , Tommaso Marchetti², Michael R. Rich¹² , Evan Butler^{1,13} , William I. Clarkson¹⁴ ,
Michael Rivet¹ , Kathryn Devine¹⁵ , A. Katherina Vivas¹⁶ , Gabriel I. Perren¹⁷ , Mario Soto¹⁸ , and Erika Silva³

¹ Saint Martin's University, 5000 Abbey Way SE, Lacey, WA 98503, USA

² European Southern Observatory, Karl-Schwarzschild-Strasse 2, D-85748 Garching bei München, Germany

³ Department of Physics & Astronomy, Western Washington University, MS-9164, 516 High Street, Bellingham, WA 98225, USA

⁴ Physics Department, Seattle University, 901 12th Avenue, Seattle, WA 98122, USA

⁵ Konkoly Observatory, HUN-REN Research Centre for Astronomy and Earth Sciences, Konkoly-Thege Miklós út 15-17, H-1121, Budapest, Hungary

⁶ CSFK, MTA Centre of Excellence, Budapest, Konkoly-Thege Miklós út 15-17, H-1121, Budapest, Hungary

⁷ Shanghai Key Lab for Astrophysics, Shanghai Normal University, 100 Guilin Road, Shanghai, 200234, People's Republic of China

⁸ Department of Mathematics, Oregon State University, 1500 SW Jefferson Way, Corvallis, OR 97331, USA

⁹ Space Telescope Science Institute, 3700 San Martin Drive, Baltimore, MD 21218, USA

¹⁰ Indiana University, Department of Astronomy, SW319, 727 E 3rd Street, Bloomington, IN 47405, USA

¹¹ Zentrum für Astronomie der Universität Heidelberg, Astronomisches Rechen-Institut, Mönchhofstr. 12-14, D-69120 Heidelberg, Germany

¹² Department of Physics and Astronomy, UCLA, 430 Portola Plaza, Box 951547, Los Angeles, CA 90095-1547, USA

¹³ Department of Astronomy, University of Washington, Physics-Astronomy Bldg, Room C319, Box 351580, Seattle, WA 98195-1700, USA

¹⁴ Department of Natural Sciences, University of Michigan-Dearborn, 4901 Evergreen Road, Dearborn, MI 48128, USA

¹⁵ The College of Idaho, 2112 Cleveland Boulevard, Caldwell, ID 83605, USA

¹⁶ Cerro Tololo Inter-American Observatory/NSF's NOIRLab, Casilla 603, La Serena, Chile

¹⁷ Instituto de Astrofísica de La Plata, IALP (CONICET-UNLP), 1900 La Plata, Argentina

¹⁸ Instituto de Astronomía y Ciencias Planetarias, Universidad de Atacama, Copayapu 485, Copiapó, Chile

Received 2023 July 27; revised 2023 October 25; accepted 2023 October 26; published 2023 December 15

Abstract

The Milky Way Bulge extra-tidal star survey is a spectroscopic survey with the goal of identifying stripped globular cluster stars from inner Galaxy clusters. In this way, an indication of the fraction of metal-poor bulge stars that originated from globular clusters can be determined. We observed and analyzed stars in and around BH 261, an understudied globular cluster in the bulge. From seven giants within the tidal radius of the cluster, we measured an average heliocentric radial velocity of $\langle RV \rangle = -61 \pm 2.6 \text{ km s}^{-1}$ with a radial velocity dispersion of $\langle \sigma \rangle = 6.1 \pm 1.9 \text{ km s}^{-1}$. The large velocity dispersion may have arisen from tidal heating in the cluster's orbit about the Galactic center, or because BH 261 has a high dynamical mass as well as a high mass-to-light ratio. From spectra of five giants, we measure an average metallicity of $\langle [Fe/H] \rangle = -1.1 \pm 0.2 \text{ dex}$. We also spectroscopically confirm an RR Lyrae star in BH 261, which yields a distance to the cluster of $7.1 \pm 0.4 \text{ kpc}$. Stars with 3D velocities and metallicities consistent with BH 261 reaching to ~ 0.5 from the cluster are identified. A handful of these stars are also consistent with the spatial distribution of potential debris from models focusing on the most recent disruption of the cluster.

Unified Astronomy Thesaurus concepts: [Stellar populations \(1622\)](#); [Galactic archaeology \(2178\)](#); [Milky Way dynamics \(1051\)](#); [Galactic bulge \(2041\)](#); [Galaxy bulges \(578\)](#); [Globular star clusters \(656\)](#); [Stellar accretion \(1578\)](#)

Supporting material: machine-readable tables

1. Introduction

The connection between globular clusters (GCs) in the inner Galaxy and the hierarchical growth of the Milky Way (MW) is still largely unknown. One reason why bulge GCs are difficult to place into proper context within our Galaxy's formation is that they often have features not seen in the GC halo or disk population. For example, Terzan 5 and Liller 1 are bulge GC fossil fragments that host an old ($\sim 12 \text{ Gyr}$) and young ($\sim 1\text{--}3 \text{ Gyr}$) stellar population (e.g., Ferraro et al. 2021). NGC 6441 and NGC 6388 are bulge GCs with abnormal horizontal branches—too blue and extended for their $[Fe/H]$ metallicities and with abnormal frequencies and pulsation properties in their RR Lyrae populations (Pritzl et al. 2000, 2001).

The Galactic bulge is home to the most metal-rich GCs in our Galaxy, and studies of the elemental abundances (e.g., O and Na) in bulge GC stars indicate that the evolution of many bulge GCs is not similar to that of the halo (e.g., Muñoz et al. 2017).

In particular, the metal-poor stars in the field of the bulge appear to be connected to inner Galaxy GCs. Field stars with $[N/Fe]$ overabundances are thought to be former members of a population of GCs that was previously dissolved and/or evaporated (e.g., Schiavon et al. 2017; Fernández-Trincado et al. 2021). This is the same mechanism that has been shown to donate stars to the halo (e.g., Martell et al. 2011; Koch et al. 2019). Stripped GC stars are also contenders for the origin of the double red clump feature in the bulge, as it has been shown that the chemical abundances of the stars in the X-shaped bulge are consistent with having been formed from GC fossil remnants (Lim et al. 2021). Although it is expected that Galactic GCs lose mass through processes such as evaporation and tidal stripping (e.g., Leon et al. 2000; Baumgardt &

Makino 2003; Moreno et al. 2014; Baumgardt & Vasiliev 2021), the extent of stripped GC stars in the bulge is unclear. Yet in the bulge, where dynamical friction is much higher than in the halo, this process is likely a significant mechanism of the makeup of the bulge field, especially for the metal-poor bulge population.

One hindrance in being able to draw connections between inner Galaxy GCs and place this population into context with Milky Way formation is that these are dense systems in a crowded, extinguished part of the Milky Way, so observational analysis of the inner Galaxy GCs is difficult. Many of them are understudied, with basic parameters such as radial velocities and metallicities being undetermined, prompting new spectroscopic surveys to target inner Galaxy GCs (e.g., Saviane et al. 2012; Dias et al. 2016; Geisler et al. 2021; Kunder et al. 2021). The Milky Way Bulge extra-tidal star survey, MWBest, has the goal of spectroscopically identifying stripped globular cluster stars from inner Galaxy clusters. Globular cluster stars can and will escape close to the tidal boundary of the cluster as it moves through the inner Galaxy, influenced by the tidal force of the Milky Way, but detections of stripped globular cluster stars in the inner Galaxy are few (e.g., Gnedin & Ostriker 1997; Leon et al. 2000; Kunder et al. 2014, 2018; Minniti et al. 2018; Kundu et al. 2019). The tidal force inflates the cluster (tidal heating), and tidal stripping removes mass from its outer region. Due to the severe crowding of the bulge, we concentrate on potential extra-tidal stars that lie a few tidal radii ($\sim 1\text{--}5 \times r_t$) away from the cluster center.

This paper focuses on the bulge globular cluster BH 261. Andrews & Lindsay (1967) list it as AL 3, van den Bergh & Hagen (1975) list it as BH 261, and Lauberts (1982) lists it as ESO456-SC78. The first color–magnitude diagrams (CMDs) of this region by Carraro et al. (2005) show very little evidence that it is a true cluster. It was the photometry presented in Ortolani et al. (2006) that allowed this cluster to be confirmed as a GC, and provided a photometric distance, reddening, and metallicity from isochrone fitting. A deep CMD of BH 261 is presented by Cohen et al. (2018), who confirm a sparse, blue horizontal branch morphology using the Hubble Space Telescope. Since then, new photometry from Gaia (Gaia Collaboration et al. 2016, 2021) and the VISTA Variables in the Via Lactea (VVV) survey (Minniti et al. 2010) has been presented by Gran et al. (2022), finding a photometric distance that places the cluster 50% further away, on the far side of the bulge, and a photometric metallicity that is a factor of 10 more metal-poor.

Spectroscopic studies of stars in BH 261 include those by Baumgardt et al. (2019), Barbuy et al. (2021), and Geisler et al. (2023), who report an average radial velocity of -29.4 km s^{-1} , $-57.9 \pm 4.3 \text{ km s}^{-1}$, and $-44.9 \pm 3.8 \text{ km s}^{-1}$, respectively. One reason for these differing results may be the small sample sizes (~ 3 stars in each study), or it could be that BH 261 has a larger velocity dispersion than can be reported with the small sample sizes. The spectroscopic $[\text{Fe}/\text{H}]$ of BH 261 is measured to be between ~ -1.0 and ~ -1.3 (Barbuy et al. 2021; Geisler et al. 2023), also based on three member stars.

The spectroscopic observations presented here allow a more detailed dynamical study to be carried out, since our observations extend out to $\sim 2^\circ$ from the cluster center, or ~ 20 tidal radii. The new data collected are described in Section 2, and the radial velocities and metallicities are presented in Section 3. In Section 3.4 the extra-tidal stars

identified are compared to theoretical predictions of tidal debris from the initial conditions of BH 261, and a comparison between BH 261 and other bulge GCs is carried out. The conclusions are in Section 4.

2. Observations and Data Reductions

2.1. Target Selection

BH 261 is heavily contaminated by both Galactic disk stars and bulge field stars, which makes efficient target selection difficult. The Gaia catalog (Gaia Collaboration et al. 2023) was used to apply proper motion and parallax criteria to select stars consistent with the cluster and to cull both foreground and field stars, as shown in Figure 1. In particular, stars with proper motions within $\mu_\alpha \pm 1.5 \text{ mas yr}^{-1}$ and $\mu_\delta \pm 1.5 \text{ mas yr}^{-1}$ of the mean proper motion of the cluster were selected, where the mean proper motion of BH 261 is $\mu_\alpha \cos \delta = 3.589 \pm 0.022 \text{ mas yr}^{-1}$, $\mu_\delta = -3.570 \pm 0.020 \text{ mas yr}^{-1}$ (Vasiliev & Baumgardt 2021). Stars with parallax values larger than 0.4 mas were discarded, as it was shown that these stars in general are part of the foreground disk (Marchetti et al. 2022). Proper motion and parallax information is not precise enough for cluster membership of BH 261; our derived radial velocities are ultimately used to select the most likely cluster members.

The Blanco DECam Bulge Survey (BDBS) catalog (Johnson et al. 2020; Rich et al. 2020) was also used to select targets for the cluster, selecting stars with u and i photometry that would, in principle, encompass the cluster’s red giant branch and blue horizontal branch (BHB). BDBS is a photometric survey covering more than 200 square degrees of the Southern Galactic bulge using the $ugrizY$ filters on the Dark Energy Camera. Photometry of approximately 250 million unique sources is available in BDBS, spanning the Galactic longitude range from $l = -10^\circ$ to $+10^\circ$ and the Galactic latitude range from $b = -3^\circ$ to -10° .

The stars assigned the highest priority were those within the tidal radius of BH 261 that were consistent with being BHB stars. Because the BHB is more offset from the bulge field population (see Figure 2), this should maximize the number of bona fide BH 261 stars. However, BHB stars have higher temperatures than giants and red giants, so the proximity to and systematic blueward offset of the calcium infrared triplet to the hydrogen Paschen lines complicates determination of stellar parameters.

We also targeted red clump stars with photometric metallicities more metal-poor than $[\text{Fe}/\text{H}] = -0.3 \text{ dex}$. Johnson et al. (2020, 2022) show that $u - i$ colors can be used to obtain color- $[\text{Fe}/\text{H}]$ relations for red clump stars good to $\sim 0.2 \text{ dex}$. This precision is comparable to that of most spectroscopic metallicities of bulge stars (see also Lim et al. 2021). The targeted stars have BDBS u -band photometry with formal uncertainties of $u_{\text{err}} < 0.024 \text{ mag}$, with the observed stars with $u \sim 18 \text{ mag}$ or brighter having $u_{\text{err}} < 0.01 \text{ mag}$.

2.2. Observations and Reduction

New spectra were collected using the AAOmega multifibre spectrograph at the 3.9 m Anglo-Australian Telescope (AAT, Siding Spring Observatory, Coonabarabran, NSW, Australia). The five-night run occurred on 2022 July 20–24 (PROP-ID: O/2022A/3002). Plate configurations for the Two Degree Field (2dF) fiber positioner contained a combination of RR Lyrae stars, red clump stars, and giants centered on the cluster and

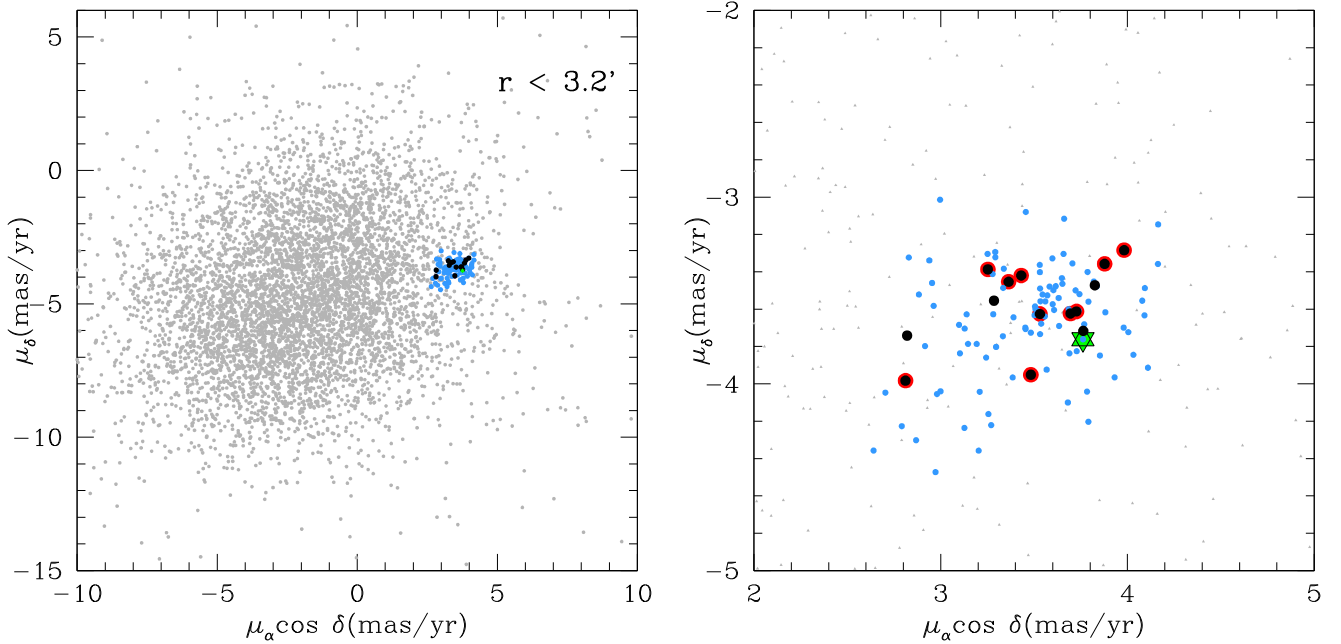


Figure 1. The Gaia proper motion distribution of the BDBS stars centered in a $3/2$ radius from BH 261. Blue points show stars with proper motions within 1.5 mas yr^{-1} in both μ_α and μ_δ of the mean proper motion of the cluster, as well as those with stars with parallax values smaller than 0.4 mas . The black points indicate stars that were spectroscopically targeted, and those with red highlights are those that were found to be radial velocity members. The star symbol (green) indicates the RR Lyrae star OGLE-BLG-RRLYR-35078.

filling the 2° field of view, as shown in Figure 3. All of the stars targeted have proper motions consistent with BH 261. The field was observed twice with two different configurations—different giant stars were observed in the two configurations to maximize number of potential cluster stars and extra-tidal stars, but the same red clump stars were observed as they are fainter, in case the spectra needed to be stacked. Also, the same RR Lyrae stars were observed in each configuration to maximize phase coverage for these pulsating variables.

A dual setup was used to employ the red 1700D grating, centered at 8600 \AA and the blue 2500V grating, centered at 5000 \AA . In this manner, the easily seen calcium triplet (CaT) lines in the red were observed, and for the brightest stars, the Mg line at 5180 \AA in the blue was prominent. This paper uses only the red part of the spectra, and any analyses of metallicities and $[\text{Mg}/\text{Fe}]$ will be presented at a later stage. The exposure times ranged from 4×30 to 2×30 minutes, adjusting for weather and observing conditions. The typical signal-to-noise ratio (S/N) was ~ 5 per pixel for the fainter horizontal branch (HB) stars and ~ 45 per pixel for the brighter giants.

The bias subtraction, cosmic-ray cleaning, quartz-flatfielding, wavelength calibration via arc-lamp exposures, sky subtraction using dedicated sky fibers, and optimal extraction of the science spectra were carried out using AAO’s 2dfdr pipeline (AAO Software Team 2015). The final wavelength range is $8350\text{--}8800 \text{ \AA}$, with slight variations depending on the exact position of the spectra on the CCD.

2.3. Radial Velocities and $[\text{Fe}/\text{H}]$ Measurements

Radial velocities were measured using IRAF’s `xcsao` routine (Tody 1986, 1993), which utilizes cross-correlation against another spectrum. The three spectra we used as cross-correlation templates were stars observed during the same run, selected from the Apache Point Observatory Galaxy Evolution

Experiment (APOGEE, Eisenstein et al. 2011) database. In particular, APOGEE 2M18134674-2926056 ($\text{RV} = 27.88 \pm 0.03$), APOGEE 2M17514997-2906055 ($\text{RV} = -187.33 \pm 0.02$), and APOGEE 2M17521244-2919510 ($\text{RV} = 65.13 \pm 0.05$) were adopted as radial velocity templates. This led to a median velocity error of $\sim 3 \text{ km s}^{-1}$ for the giants and 9 km s^{-1} for the fainter and hotter HB stars.

Two epochs of observations were collected for the RR Lyrae star OGLE-BLG-RRLYR-35078, and these are shown in Figure 4 (right panel). Each epoch of observation is phased using the OGLE pulsation ephemerides and pulsation period. To calculate the mean radial velocity, the RRc template presented in Z. Prudil et al. (2023, in preparation) is adopted. The photometric scaling relation adopted between the photometric amplitude, Amp_V , and line-of-sight velocity amplitude, Amp_{los} , is $\text{Amp}_{\text{los}} = 54(1) \times \text{Amp}_V$. This was derived specifically for RRc pulsators from five well-sampled local RR Lyrae stars observed by APOGEE (Z. Prudil et al. 2023, in preparation). For Amp_V , the OGLE I -amplitude is transformed to Amp_V using $\text{Amp}_V = 1.72 \times \text{Amp}_I$ (Kunder et al. 2013; Z. Prudil et al. 2023, in preparation). The determined systemic velocity and its uncertainty is $-39.8 \pm 12.4 \text{ km s}^{-1}$. The 12.4 km s^{-1} uncertainty in the systemic velocity comes from adding in quadrature the 9.8 km s^{-1} individual radial velocity uncertainty to the 7.6 km s^{-1} uncertainty from the model fitted to find the systemic velocity. The source of uncertainty comes from the faint magnitude of this star combined with its higher temperature. The shaded gray in Figure 4 about the scaled RRc template designates a 9.8 km s^{-1} uncertainty.

The APOGEE DR17 catalog contains a number of RR Lyrae star observations, including two epochs of observations of OGLE-BLG-RRLYR-35078. The `allVisit-r12-133.fits` file was used to extract the exact time each observation was taken as listed in the column `JD`. The Julian Date from this file refers to the middle of an exposure sequence, which is determined from the exposure-time-weighted mean of the mid-exposure times. Again

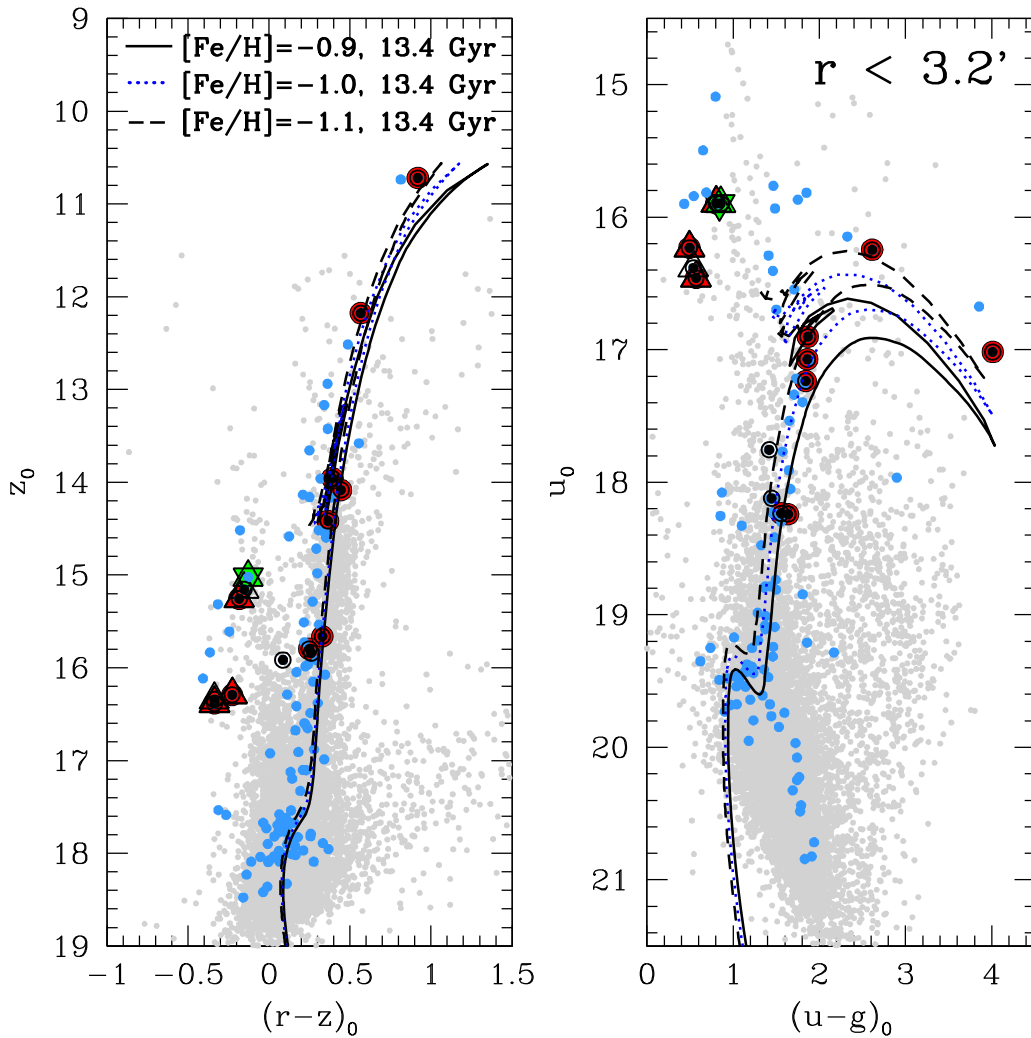


Figure 2. The BDBS color–magnitude diagram showing the horizontal branch stars (triangles), giants (circles), and RR Lyrae star (star) for which radial velocities have been determined from AAOmega@AAT. The filled red symbols indicate those stars that have radial velocities consistent with BH 261 (see Table 2), whereas the open triangle and circles are those stars that do not have velocities consistent with the cluster. The underlying BDBS stellar distribution in this field is shown with small gray points and those stars with proper motions consistent with the cluster are shown in blue. The black lines show the MIST (MESA Isochrones and Stellar Tracks, Choi et al. 2016) isochrone from which the cluster’s distance is derived in this work (7.1 kpc).

using the OGLE time of maximum brightness and OGLE period, the phase of each APOGEE RR Lyrae observation was calculated. The APOGEE radial velocity observations give a systemic velocity of $-67.2 \pm 2.3 \text{ km s}^{-1}$. The APOGEE mean velocity as well as that derived here are both consistent with the range of velocities seen for stars in BH 261. Therefore, the radial velocity also confirms that OGLE-BLG-RRLYR-35078 is a cluster member, in agreement with its proper motion and spatial proximity to the cluster.

The radial velocity of OGLE-BLG-RRLYR-35078 presented here, $-39.8 \pm 12.4 \text{ km s}^{-1}$, is used throughout the paper, as the calcium triplet lines are stronger than the spectral lines in the APOGEE H -band wavelength regime, especially at the higher temperatures of first-overtone RR Lyrae stars. Further, APOGEE’s reduction pipeline (Nidever et al. 2015) stacks all spectra of a given object to increase S/N, and a radial velocity on the stacked spectra is determined. This radial velocity is a first estimate, or a base for prior, for further determination of radial velocity for that given star. This procedure may be suboptimal for stars that change their radial velocities with amplitudes of $\sim 15\text{--}50 \text{ km s}^{-1}$ in short periods, like RR Lyrae stars. The small formal uncertainties in the

APOGEE spectra of 2.2 km s^{-1} and 1.5 km s^{-1} are almost certainly underestimated given the S/N of 4.1 and 7.6, respectively. As far as we know, this is the first publication using the APOGEE DR17 measurements of RR Lyrae stars, and we look forward to further discussion of APOGEE radial velocities for RR Lyrae stars in potential forthcoming papers.

The SP_ACE code (Boeche & Grebel 2016; Boeche et al. 2021) was utilized for the determination of $[\text{Fe}/\text{H}]$ metallicities for the giants. For the red clump stars observed, photometric metallicities were calculated from the calibration between DECam passbands and $[\text{Fe}/\text{H}]$ as presented in Johnson et al. (2020, 2022). Spectroscopic metallicities from SP_ACE are used to verify the authenticity of the red clump $[\text{Fe}/\text{H}]$ metallicities. The spectroscopic metallicities are discussed in more detail in Section 3.4.

3. BH 261 Results

3.1. Distance

The distance to BH 261 has been determined from CMD fitting and ranges from $d_{\odot} = 6.0 \pm 0.6 \text{ kpc}$ from optical CMD fitting (Ortolani et al. 2006; Barbuy et al. 2021) to d_{\odot}

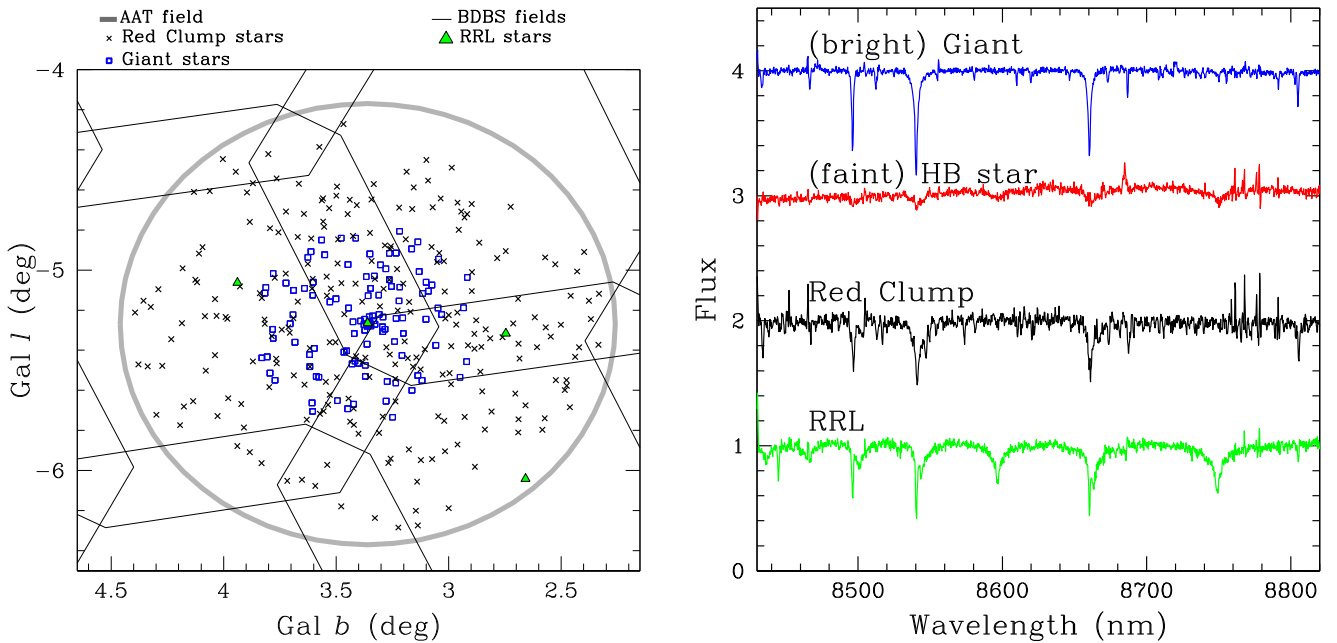


Figure 3. Left: the stars in and around BH 261 targeted spectroscopically with AAOmega@AAT. The field is centered on the GC BH 261. Right: example spectra from AAOmega illustrating the difference in quality between a bright giant ($i = 14.678$ mag), a faint HB star ($i = 16.814$ mag), a typical red clump star ($i = 16.515$ mag), and a typical red clump star ($i = 16.515$ mag). The spectra have been normalized and are offset for clarity.

= 9.12 kpc from infrared CMD fitting (Gran et al. 2022). There is unfortunately no DR3 parallax or kinematic distance for BH 261 (Baumgardt & Vasiliev 2021). The reason for the large discrepancy in distance from CMD fitting is that there is a degeneracy between metallicity and distance: adopting $[\text{Fe}/\text{H}] \sim -1.0$ leads to a distance of $d_{\odot} \sim 6.0$ kpc whereas adopting a more metal-poor $[\text{Fe}/\text{H}] \sim -2.5$ leads to a distance of $d_{\odot} \sim 9.5$ kpc. The advantage of adopting a more metal-poor value for BH 261 is that a larger distance to the cluster makes it easier to explain its large velocity dispersion despite its low luminosity, as this gives a mass-to-light ratio more in line with what is seen for typical GCs. The recent spectroscopic $[\text{Fe}/\text{H}]$ metallicities for BH 261 in Geisler et al. (2023) agree with the metallicity put forward by Barbuy et al. (2021) and Ortolani et al. (2006), making it unlikely that the further distance is appropriate.

We report an RR Lyrae star—OGLE-BLG-RRLYR-35078—that both lies 0.4 from the center of the cluster and has a proper motion consistent with BH 261. Our derived radial velocity further indicates it is a cluster member. As such, this star can provide an independent indicator to estimate the distance to BH 261.

Empirical period–absolute magnitude–metallicity (PMZ) relations for RR Lyrae stars have greatly improved, especially since the trigonometric parallaxes measured by Gaia have been released. For the determination of the distance to this RRc star, the newly calibrated PMZ relations in Prudil et al. (2023) are employed. Briefly, the calibrating data set of Prudil et al. (2023) consists of 100 RR Lyrae stars with mean magnitude, reddenings, pulsation properties, iron abundances, and parallaxes from Gaia DR3. Both RRab and RRc pulsators are included in the calibrating set and it was shown that their derived PMZ relations accurately estimate the distance moduli to NGC 6121, NGC 5139, the LMC and SMC, as well as the the prototype of RR Lyrae class, RR Lyr. Because the motivation behind the PMZ relations of Prudil et al. (2023) is

to use them for RR Lyrae stars toward the Galactic bulge, special care is taken to calibrate the relations to the OGLE and VVV photometric system directly. Further, a homogeneous metallicity scale is used for the calibrating sample that allows the direct use of photometric metallicity derived from the OGLE I -band photometry. The PMZ relations of Prudil et al. (2023) are used to investigate the distance to BH 261. Assuming $A_k = 0.04 \pm 0.02$ mag and a photometric metallicity of $[\text{Fe}/\text{H}] = -1.25$ (Dékány et al. 2021), a distance of $d = 7132 \pm 312$ pc is derived from the OGLE I band and the VVV K_s band. Using only the VVV J and K_s bands, $A_k = 0.08 \pm 0.09$ mag is found, and a distance of $d = 7006 \pm 427$ pc is derived. Throughout the paper, we adopt a distance of 7.1 ± 0.3 kpc as the distance to BH 261.

The $[\text{Fe}/\text{H}] = -1.25$ metallicity of Dékány et al. (2021) for the BH 261 RR Lyrae star is based on the metallicity scale of For et al. (2011), Chadid et al. (2017), Sneden et al. (2017), and Crestani et al. (2021), abbreviated as CFCS. This is different than the SP_ACE and APOGEE metallicity scale. To quantify the difference between these two metallicity scales, the average Dékány et al. (2021) metallicity of RR Lyrae stars in the bulge GCs with at least six RR Lyrae stars is determined. Two of those GCs have published $[\text{Fe}/\text{H}]$ abundances from APOGEE’s ASPCAP. NGC 6642 has an APOGEE-derived $[\text{Fe}/\text{H}] = -1.11$ (Geisler et al. 2021) and 19 OGLE RR Lyrae stars with an average CFCS photometric $[\text{Fe}/\text{H}] = -1.42$. FSR 1758 has an APOGEE-derived $[\text{Fe}/\text{H}] = -1.43$ (Romero-Colmenares et al. 2021) and nine OGLE RR Lyrae stars with an average CFCS photometric $[\text{Fe}/\text{H}] = -1.84$. Therefore, the photometric metallicities of RR Lyrae stars are ~ -0.3 dex more metal-poor than the APOGEE ASPCAP $[\text{Fe}/\text{H}]$ metallicity. The RR Lyrae metallicity of BH 261 of $[\text{Fe}/\text{H}] = -1.25$ corresponds to $[\text{Fe}/\text{H}] = -0.95$ dex on the APOGEE/ASPCAP scale, in agreement with the SP_ACE-derived metallicity of BH 261 giants in Section 3.4.

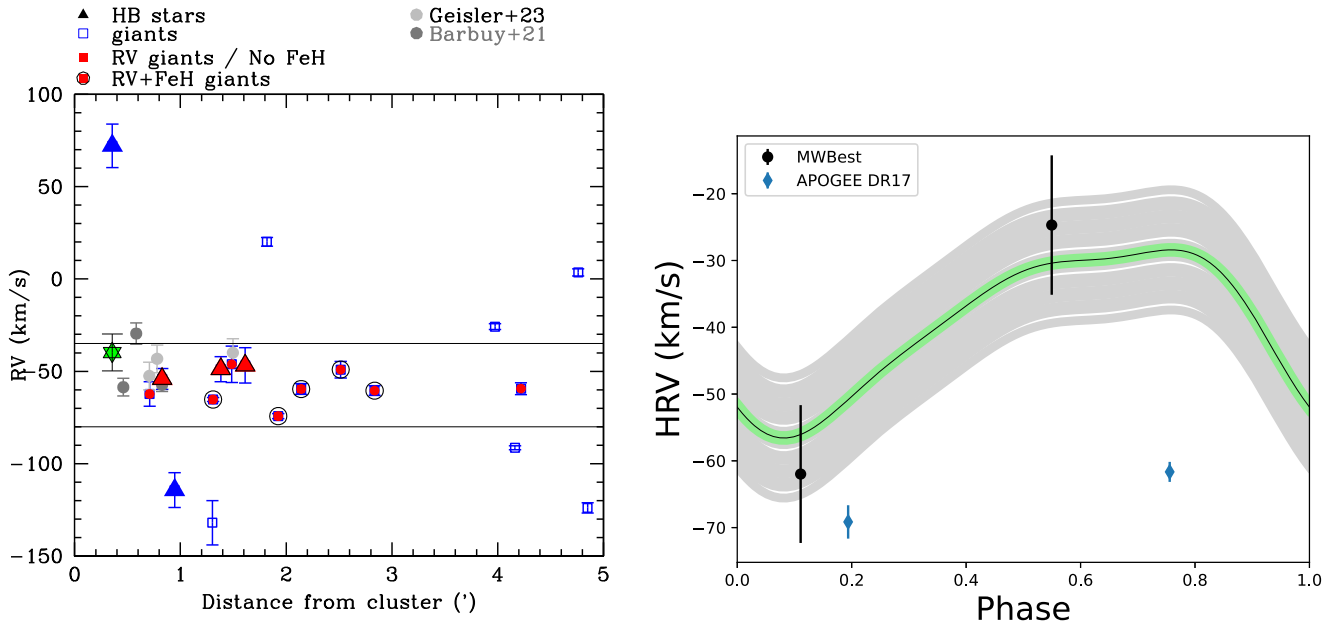


Figure 4. Left: the heliocentric velocities of our targeted stars within $5'$ of BH 261. The clump of 12 stars with radial velocities of $\sim -60 \text{ km s}^{-1}$ within the $3/5$ of the cluster are consistent with being BH 261 stars. Right: the radial velocity curve of the first-overtone RR Lyrae, OGLE-BLG-RRLYR-35078, which has both a proper motion and a radial velocity consistent with BH 261. The RRc template from Z. Prudil et al. (2023, in preparation) is used to obtain a center-of-mass radial velocity. The APOGEE DR17 observations are also shown, but not used in determining the radial velocity.

3.2. Color–Magnitude Diagram

The BDBS photometry combined with Gaia astrometry allows a modern optical CMD of BH 261 to be constructed, and so we focus first on the cluster itself in an effort to validate the cluster parameters determined independently without the use of BDBS photometry (e.g., distance and metallicity). Figure 2 shows the dereddened proper-motion-cleaned u_0 versus $(u - g)_0$ and r_0 versus $(r - z)_0$ CMD of a region within $3/2$ of BH 261. A $3/2$ radius is chosen because it is large enough to encompass enough cluster and field BDBS stars to see a differentiation between the two when separated by proper motion, and it is also small enough where most of the radial-velocity-confirmed cluster stars are present (see Figure 4). All stars have been dereddened using the extinctions from the Simion et al. (2017) reddening map, which has a resolution of $1' \times 1'$. The reddening vectors were computed using Green et al. (2018) for the *grizy* bands and Schlafly & Finkbeiner (2011) for the *u* band, as outlined in Johnson et al. (2020). The Green et al. (2018) extinction vector is preferred as it is based on a combination of broadband stellar colors and APOGEE spectra, where most of the APOGEE reference stars used belong to the disk and bulge. Kader et al. (2023) derive high-resolution extinction maps for 14 GCs in BDBS and show that these reddening maps are in agreement with the VVV map used here. Still, we note that the *u*-band extinction vector is notoriously difficult to calibrate, and large uncertainties in the *u*-band extinction can arise from small variations in the reddening law between different lines of sight. The range of extinction values within the central $3/2$ of BH 261 varies from $E(B - V) \simeq 0.25$ to 0.36 , with a mean of $E(B - V) = 0.29 \text{ mag}$.

The isochrones used are from the publicly available Modules for Experiments in Astrophysics (MESA) Isochrones and Stellar Tracks (MIST) database (Choi et al. 2016). The isochrones were transformed from theoretical coordinates to the appropriate bandpasses using a combination of the Sloan Digital Sky Survey and PanSTARRS color transformation

schemes. The α -element enhancement is accounted for following the procedure described in Joyce et al. (2023). The shorter-wavelength passbands (e.g., *u* band) allow for the largest discrimination between isochrones with, e.g., different metallicities and ages, but shorter-wavelength passbands are also more sensitive to variations in reddening and extinction, as discussed above.

The isochrones with metallicities of $[\text{Fe}/\text{H}] \sim -0.9$ to $[\text{Fe}/\text{H}] \sim -1.1$ dex with an old age (~ 13 – 13.5 Gyr) are in agreement with the *u - g* CMD. A 13.4 Gyr isochrone age was used to be similar to the 13.4 ± 1 Gyr estimated by Barbuy et al. (2021). Most bulge GCs with $[\text{Fe}/\text{H}] \sim -1.0$ and a BHB have ages in this range (e.g., Kerber et al. 2018), and it has been shown that one avenue to produce such metal-rich GCs with a BHB is by them being very old (e.g., Lee et al. 1994). We note that very low metallicities are not needed for stellar relics in the bulge—the chemical enrichment of the bulge is faster than in many other places in the MW (e.g., Zoccali et al. 2006; Bensby et al. 2013), and a flat age–metallicity relation for inner Galaxy GCs has been established (Marín-Franch et al. 2009; Massari et al. 2019).

The radial velocity members falling along the BHB of the cluster (see Figure 2) confirm that BH 261 does have an extended BHB, despite it being relatively metal-rich. It has been suggested that BH 261’s broad HB could be due to a number of blue straggler stars. Although this may be the case, we find that the contamination in this region of the CMD from field stars is not trivial. From our sample of five spectroscopically targeted possible BHB stars (all with proper motions consistent with BH 261), 2/5 have radial velocities excluding them from being cluster members. This ratio is similar to the giant stars we targeted and highlights the difficulty of obtaining clean cluster samples from proper motions and position on the CMD alone.

The *ugrizY* BDBS photometry of all stars within $3/2$ of BH 261 is presented in Table 1.

3.3. Velocities

The derived radial velocities as a function of distance from the cluster center are shown in Figure 4 (left panel). There is a grouping of stars within $4'$ of the cluster with radial velocities between -35 and -80 km s^{-1} , which we consider the most probable member stars currently within BH 261. To search for systematic offsets between different samples of BH 261 stars, our stars are cross-matched with the sample presented in Geisler et al. (2023) and Barbuy et al. (2021). There are two stars in our sample that overlap with those in Geisler et al. (2023)—Gaia-4050600806719928576 and Gaia-4050624308743727744. The radial velocities presented here agree within 1σ with the radial velocities reported in Table 2 of Geisler et al. (2023), both when the total velocity error of 7.5 km s^{-1} is adopted for the Geisler et al. (2023) measurements (which arises from the error in centering the image in the spectrograph combined with the standard deviation of the different cross-correlations) and when the smaller, statistical errors in velocity of $\sim 2 \text{ km s}^{-1}$ are adopted.

The most probable cluster members of BH 261 are listed in Table 2, along with (1) the Gaia DR3 ID of each star, (2) the R.A. of the star from Gaia, (3) the decl. of the star from Gaia in degrees, (4) the proper motion in the R.A. direction as provided by Gaia ($\mu_\alpha^* = \mu_\alpha \cos \delta$), (5) the proper motion in decl. as provided by Gaia, (6) the heliocentric radial velocity (HRV), (7) the [Fe/H] metallicity from SP_ACE, and (8) the distance the star is from the cluster center.

The [Fe/H] metallicities of these stars, as discussed in Section 3.4 below, are also consistent with being more metal-poor than the field population. Therefore, the stars most likely currently within the cluster BH 261 (1) are within the cluster tidal radius, (2) have an RV that falls within the error plus intrinsic dispersion (generously adopted as $\pm 15 \text{ km s}^{-1}$) from the cluster mean, (3) have an [Fe/H] value within ± 0.3 dex of the mean metallicity of the cluster, and (4) have a proper motion that lies within two standard deviations from the cluster mean. These criteria have been used by a number of similar studies discriminating between bulge cluster members and surrounding field stars (e.g., Dias et al. 2022; Parisi et al. 2022; Geisler et al. 2023).

The mean velocity of these 12 stars is $\langle \text{RV} \rangle = -56 \pm 3 \text{ km s}^{-1}$ with a radial velocity dispersion of $\langle \sigma \rangle = 7.0 \pm 1.9 \text{ km s}^{-1}$. This velocity dispersion is higher than reported in previous studies, but is also based on a sample size that is a factor of 4 larger. Although most foreground stars should be distinguishable with parallax, background stars are not. By removing the star with the most negative radial velocity, a star $1.9'$ from the cluster center, a mean velocity of $\langle \text{RV} \rangle = -54 \pm 2 \text{ km s}^{-1}$ with a radial velocity dispersion of $\langle \sigma \rangle = 5.0 \pm 1.7 \text{ km s}^{-1}$ is found. This brings down the velocity dispersion. Note that this star has a [Fe/H] metallicity consistent with the metallicity of BH 261, and is more metal-poor than the field, which is why it is still included as a potential cluster member. Removing the horizontal branch stars, which have larger radial velocity uncertainties, as well as one giant with a radial velocity uncertainty of 10 km s^{-1} , the mean velocity is $\langle \text{RV} \rangle = -61 \pm 2.6 \text{ km s}^{-1}$ with a radial velocity dispersion of $\langle \sigma \rangle = 6.1 \pm 1.9 \text{ km s}^{-1}$.

Including the other four independent radial velocity measurements—three stars from Barbuy et al. (2021) and one from Geisler et al. (2023)—gives a sample of 16 stars. We then remove the stars with both the highest and lowest velocities to

obtain a mean velocity of $-53.6 \pm 2.0 \text{ km s}^{-1}$ with a dispersion of $5.9 \pm 1.9 \text{ km s}^{-1}$.

There may be other stars belonging to BH 261, as stars with radial velocities in this range exist out to as far as our observations go. Before evaluating the likelihood of extra-tidal stars around BH 261, [Fe/H] metallicities are calculated.

Figure 5 shows the Milky Way GCs analyzed in Baumgardt & Hilker (2018) with measured absolute magnitudes and intrinsic velocity dispersion values. The σ_0^2 parameter comes from the equation $\sigma_0^2 = \sigma_{\text{vel}}^2 - \sigma_{\text{errors}}^2$, where σ_{vel} is the standard deviation of the radial velocity distribution of the cluster members and σ_{errors} is the mean error of the velocity measurements. Using the radial velocity measurements from the 11 red clump and giant stars¹⁹ gives $\log \sigma_0^2 = 1.7 \text{ km s}^{-1}$. Removing the two stars in the sample with the highest and lowest radial velocities gives $\log \sigma_0^2 = 1.3 \text{ km s}^{-1}$.

A value of velocity dispersion based on the spread in the proper motions only can also be calculated. Because the proper motions are derived independently from the radial velocities presented here, this could be a further check of the validity of our radial velocities. In this case, the Gaia proper motions are converted into tangential velocities (v_t) in km s^{-1} using the $d = 7100 \text{ pc}$ distance found here and the relation $v_t = 4.74\mu d$, where μ is the total proper motion in arcsec yr^{-1} and 4.74 is the conversion of distance (pc to km), angle (from arcsec to radians), and time (from years to seconds). We similarly recover $\log \sigma_0^2 = 1.5 \text{ km s}^{-1}$. If the radial velocity membership criterion adopted here is too generous, the radial velocity outliers do not significantly affect the $\log \sigma_0^2$ value of the cluster, as supported by the independent σ_0 value determined from proper motion measurements.

Figure 5 indicates that inner Galaxy GCs typically have larger internal velocity dispersions at the same luminosity than GCs in the halo and disk. BH 261 is anomalous in that it has an internal velocity dispersion that generally is in line for clusters with brighter intrinsic magnitudes. The paucity of bulge GCs with $M_V > -6$ is likely due to the difficulty of detecting and studying low-luminosity GCs in the crowded and heavily extinguished bulge. The analysis presented here improves the properties of BH 261, which is especially important in the low-luminosity GC regime.

3.4. [Fe/H] Metallicities

The near-infrared region around the CaT is ideal for the determinations of radial velocities due to the strong CaT lines. There is also spectral information in this regime that can be used to constrain temperature, gravity, and chemical abundances (e.g., Ruchti et al. 2010; Koch et al. 2017). The SP_ACE code (Boeche & Grebel 2016; Boeche et al. 2021) was designed to derive stellar parameters and chemical abundances over the spectral resolution interval $R = 2000\text{--}40,000$ and over the wavelength intervals $4800\text{--}6860$ and $8400\text{--}8924 \text{ \AA}$. It was originally developed for determination of elemental abundances for the Radial Velocity Experiment (RAVE; Kunder et al. 2017; Steinmetz et al. 2020), which covers the same wavelength range as the spectra collected here. Although SP_ACE can be used to measure individual abundances for different chemical species (Mg, Al, Si, Ca, Ti, Fe, and Ni), only [Fe/H] abundances are presented here. The lower S/Ns of the spectra give the most reliable results for

¹⁹ We neglect the RR Lyrae star due to its large radial velocity uncertainty.

Table 1
BDBS Photometry of Stars within $3\frac{1}{2}$ from BH 261

Gaia ID (1)	R.A. (deg) (2)	Decl. (deg) (3)	u (4)	u_{err} (5)	g (6)	g_{err} (7)	r (8)	r_{err} (9)	i (10)	i_{err} (11)	z (12)	z_{err} (13)	y (14)	y_{err} (15)
4050647188105074639	273.46301	-28.67483	21.931	0.018	20.106	0.019	19.503	0.03	19.061	0.023	18.966	0.038	18.937	0.009
4050647879579387008	273.46301	-28.63367	20.758	0.009	18.013	0.021	16.918	0.004	16.532	0.001	16.295	0.001	16.096	0.003
4050647192336176640	273.46302	-28.666	NaN	NaN	19.253	0.041	19.081	0.003	18.8	NaN	18.719	0.004	18.699	0.036
4050648051378176128	273.46305	-28.61794	21.007	0.016	19.4	0.007	18.645	0.005	18.434	0.016	18.263	0.046	18.333	0.009
4050648051330018176	273.46309	-28.61518	18.898	0.012	16.4	0.008	15.408	NaN	14.963	0.011	14.611	0.031	14.448	0.051

Note. Only a small portion of the table is shown here for clarity and the full table is available online.

(This table is available in its entirety in machine-readable form.)

∞

Table 2
Positions, Gaia Proper Motions, Radial Velocities, and [Fe/H] Metallicities of the Probable Member Stars of BH 261

Gaia ID (1)	R.A. (deg) (2)	Decl. (deg) (3)	μ_α (mas s ⁻¹) (4)	μ_δ (mas s ⁻¹) (5)	HRV (km s ⁻¹) (6)	[Fe/H] (7)	r (arcmin) (8)
4050671244212595584	273.525876	-28.601011	3.431 ± 0.084	-3.410 ± 0.064	-59.6 ± 2.9	-0.69 ± 0.2	2.14
4050624029553084928	273.562146	-28.638807	3.727 ± 0.052	-3.612 ± 0.038	-60.5 ± 2.6	-1.13 ± 0.2	2.84
4050671278572353536	273.508670	-28.614204	3.254 ± 0.042	-3.387 ± 0.033	-65.3 ± 1.1	-1.11 ± 0.2	1.31
4050624205664391040 ^{HB}	273.537938	-28.638492	2.811 ± 0.145	-3.983 ± 0.109	-48.8 ± 6.7	...	1.38
4050624274430501248 ^{HB}	273.527754	-28.640416	3.695 ± 0.057	-3.623 ± 0.043	-54.1 ± 5.6	...	0.83
4050647707732147456 ^{HB}	273.493876	-28.651595	3.878 ± 0.093	-3.358 ± 0.073	-46.8 ± 9.5	...	1.61
4050647772223823488	273.484421	-28.625506	3.982 ± 0.085	-3.284 ± 0.071	-74.3 ± 1.3	-1.37 ± 0.2	1.93
4050600806719928576	273.517931	-28.646514	3.483 ± 0.059	-3.951 ± 0.048	-62.3 ± 6.6	...	0.71
4050624308743727744	273.536860	-28.623270	3.364 ± 0.064	-3.453 ± 0.050	-46.2 ± 9.9	...	1.49
4050647669052101248	273.473132	-28.636323	3.531 ± 0.029	-3.626 ± 0.024	-49.1 ± 4.5	-1.07 ± 0.2	2.52
4050671823952489088	273.549330	-28.573736	3.558 ± 0.035	-3.585 ± 0.027	-59.5 ± 3.2	...	4.22
4050624270079129216 ^{RR}	273.520749	-28.633437	3.762 ± 0.052	-3.761 ± 0.040	-39.8 ± 12.4	...	0.36

^{HB} Horizontal branch star
^{RR} RR Lyrae star

(This table is available in machine-readable form.)

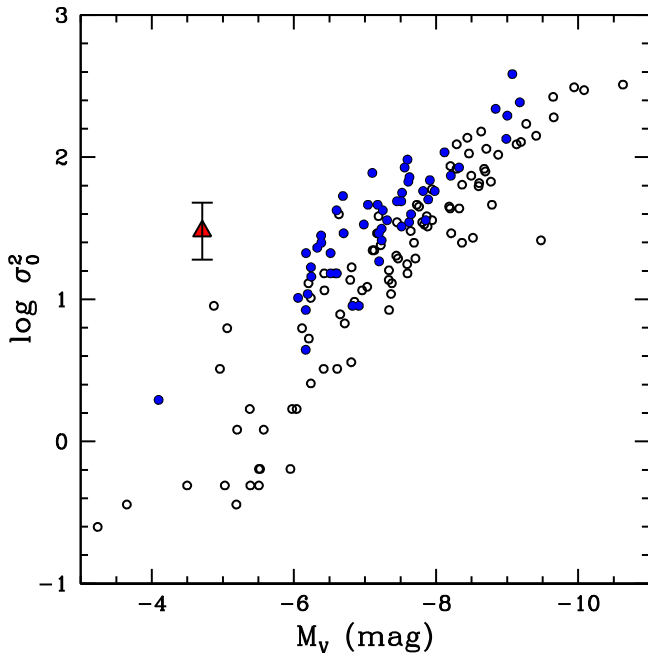


Figure 5. Absolute integrated magnitude (M_V) and velocity dispersion ($\log \sigma_0^2$) for clusters analyzed by Baumgardt & Hilker (2018). The open black points indicate globular clusters that are further than 3.35 kpc from the Galactic center, whereas the filled blue points indicate globular clusters in the inner Galaxy—those with galactocentric distances less than 3.35 kpc. The red triangle designates BH 261.

the Fe I and Fe II lines, which are the most numerous in our wavelength regime. SP_ACE was fitted to the 8450–8493, 8503–8535, 8550–8660, and 8670–8800 Å wavelength regimes in order to avoid the strong CaT lines that often cause difficulties in precise abundances and determination of stellar parameters.

The wide coverage of APOGEE stars in the inner Galaxy allowed us to allocate a few fibers in our science fields to the reobservation of APOGEE bulge giants. The higher resolution of the APOGEE spectra ($R \sim 22,000$ versus our $R \sim 10,000$ spectra) as well as the high S/N for APOGEE stars (~ 100 – 200) made it advantageous to use these as calibration standards. In total, nine bulge giants in the APOGEE survey

were observed during our run with our particular setup; they all have measured stellar parameters released in DR17 and span a wide range of [Fe/H] metallicities (see Figure 6). We also incorporated six APOGEE stars that were observed in previous AAT runs by our group with the same AAOmega setup to use as calibration standards.

Figure 6 (right panel) shows the SP_ACE [Fe/H] metallicities as compared to those published by APOGEE. The temperature and gravity regimes of SP_ACE are $T_{\text{eff}} = [3600, 7400]$ K and $\log g = [0.2, 5.0]$. For the two APOGEE stars with temperatures that are a few hundred kelvin lower than 3600 K, SP_ACE did not converge, and therefore not all APOGEE stars observed were able to serve as metallicity standards. The uncertainty in [Fe/H] from SP_ACE as compared to the APOGEE metallicities is ~ 0.2 dex. There is an indication that SP_ACE underpredicts [Fe/H] for high-metallicity stars and overpredicts it in the low-metallicity regime, but SP_ACE is able to reproduce [Fe/H] of our observed spectra between ~ -0.9 and $\sim +0.2$ dex.

None of the three observed BHB stars have SP_ACE metallicities that could be measured, since BHB stars have temperatures higher than ~ 8000 K. Also, hot BHB stars can have atmospheric effects such as levitation and diffusion that mask their true abundances. SP_ACE did converge to provide an estimate of [Fe/H] for five of the eight noncalibrating giants observed. The other three giants have a low S/N, which was likely why SP_ACE failed to provide metallicities for them. A weighted-mean metallicity of $\langle [\text{Fe}/\text{H}] \rangle = -1.07 \pm 0.22$ is found. No evidence of a spread in the metallicity in BH 261 is seen, but our sample size is small and our formal [Fe/H] uncertainty is 0.2 dex.

3.5. Extra-tidal Stars

In order to find signatures of BH 261 dissolving in the strong tidal field of the Milky Way, the tidal radius of the cluster needs to be known. Unfortunately the tidal radius of BH 261 is uncertain. There are difficulties in defining the tidal radius, both theoretically and observationally, and although there are correlations between the calculated theoretical and observational radii, it is not uncommon to find discrepancies between estimates of tidal radii when using theoretical and observational approaches (e.g., Moreno et al. 2014). Ortolani et al. (2006)

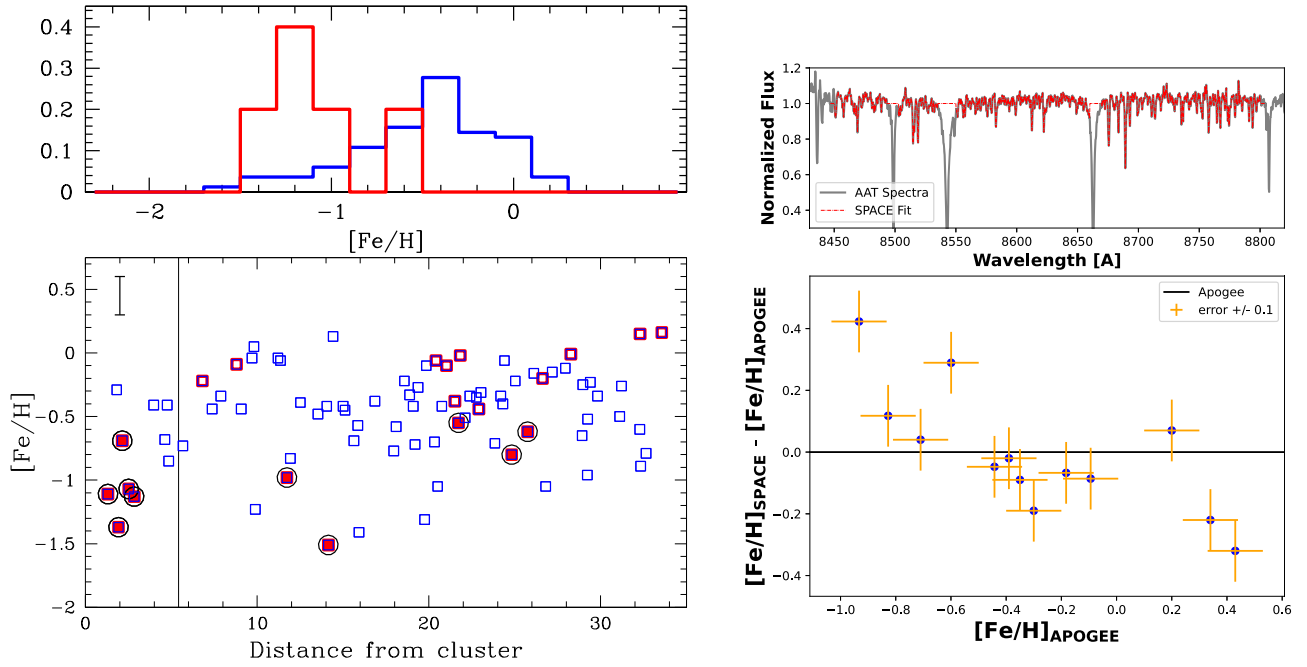


Figure 6. Left: a histogram, in blue, of the $[\text{Fe}/\text{H}]$ metallicity of our targeted stars as determined from SP_ACE. Five giant stars within the cluster tidal radius with radial velocities consistent with the cluster are highlighted in red. There are five giants with both $[\text{Fe}/\text{H}]$ metallicities and radial velocities outside the tidal radius; these are candidate extra-tidal giant stars. The tidal radius determined here (Section 3.5) is indicated by the solid line at a distance of $5\prime.4$ from the cluster center. Top right: the observed sample spectra (black) of bh261_1_197 fits of the BH 261 giants within the tidal radius of the cluster. The best-fit spectrum from SP_ACE is overlaid in red, where only the portion of the spectrum sampled by SP_ACE is shown. Note that the Campos wavelength axis used here extends to a longer wavelength range than used in Koch et al. (2017). Bottom right: a comparison between seven APOGEE bulge giants and $[\text{Fe}/\text{H}]$ derived from SP_ACE using the Campos wavelength range.

find the density profile merges with the background at $3\prime.4 \pm 0\prime.4$, and the 2010 edition of the Harris (1996) catalog lists a tidal radius of $4\prime$ for BH 261. The tidal radius listed in Baumgardt & Vasiliev (2021) is 20.63 pc, which at the distance listed in their catalog (6100 pc) corresponds to $11\prime.6$.

We use ASteCA (Automated Stellar Cluster Analysis) with the BDBS photometry combined with Gaia astrometry in an attempt to obtain an estimate of the tidal radius of BH 261. ASteCA is a Python code (Perren et al. 2015) designed to perform a thorough analysis of star clusters (open or globular), modeling spatial, structural, and photometric parameters. ASteCA can determine cluster membership probabilities by utilizing a decontamination algorithm. It allows estimation of the center and radius of the cluster, along with density profiles, luminosity functions, and color–magnitude diagrams to study the stellar population within the cluster.

ASteCA was fed 7215 stars from BDBS with useful photometry and Gaia astrometry that are within $30\prime$ from the center of BH 261. The sample of stars was constrained to have $0.0 \text{ mas yr}^{-1} < \mu_\alpha < +5.0 \text{ mas yr}^{-1}$ and $0.0 \text{ mas yr}^{-1} > \mu_\delta > -5.0 \text{ mas yr}^{-1}$, as well as parallax $< 0.4 \text{ mas}$, in an attempt to minimize field star contamination. In total, ASteCA was run ~ 30 times, utilizing different BDBS and Gaia color-combination CMDs, with tightening proper motion limits. The solutions for the physical parameters derived from the King models (King 1962, 1966) remained stable once we tightened the proper motion limits. We used the extinction corrections from Simion et al. (2017).

Limiting the proper motion to $+2.0 < \mu_\alpha < +5.0$ and $-2.5 > \mu_\delta > -4.5$ produced 5596 BDBS stars, and does not change the ASteCA-determined cluster parameters significantly. The ASteCA fit for the King model for an example of the BDBS photometry (with Gaia proper motions) is shown in

Figure 7; it produced an isochrone fit for u_0 versus $(u - z)_0$, and returned the core, cluster, and tidal radii as $r_c = 0.34^{+0.44}_{-0.28}$, $r_{cl} = 2.60^{+2.79}_{-2.45}$, and $r_t = 5.42^{+6.93}_{-4.04}$. Using the latter proper motion limits, the averages for the six final runs were $r_c = 0\prime.352 \pm 0\prime.004$, $r_{cl} = 2\prime.58 \pm 0\prime.001$, and $r_t = 5\prime.377 \pm 0\prime.080$.

ASteCA is not the ideal tool for discerning extra-tidal structures, as the decontamination procedure uses the field stars outside the cluster radius to determine the cluster membership. However, the code’s unbiased method of determining cluster parameters is useful for defining the radial density profile of the cluster and its members, thereby giving an indication of the tidal radius of the cluster.

We search for extra-tidal stars by targeting red clump stars as well as giants with proper motions consistent with BH 261. Figure 8 (left panel) shows the velocities of all giants and red clump stars targeted spectroscopically. These all have proper motions consistent with BH 261 (see Figure 1) and reach to $65\prime$ from the center of the cluster. This corresponds to approximately 6–10 times the cluster’s tidal radius, depending on the exact calculation used for the tidal radius.

Our observations detect BH 261 stars with distances out to $\sim 4\prime$ from the cluster center, but beyond this distance there is no clear overdensity of stars with radial velocities consistent with BH 261. There are a few giants and red clump stars with velocities similar to BH 261 between $5\prime$ and $10\prime$ from the cluster center, but these have metallicities that are more in line with the bulge field as opposed to a GC. Beyond a distance of $10\prime$ from the cluster center, a handful of stars are identified that have both radial velocities and $[\text{Fe}/\text{H}]$ metallicities consistent with BH 261. The most likely candidate extra-tidal stars have both radial velocities and SP_ACE metallicities consistent with BH 261; these are listed in Table 3.

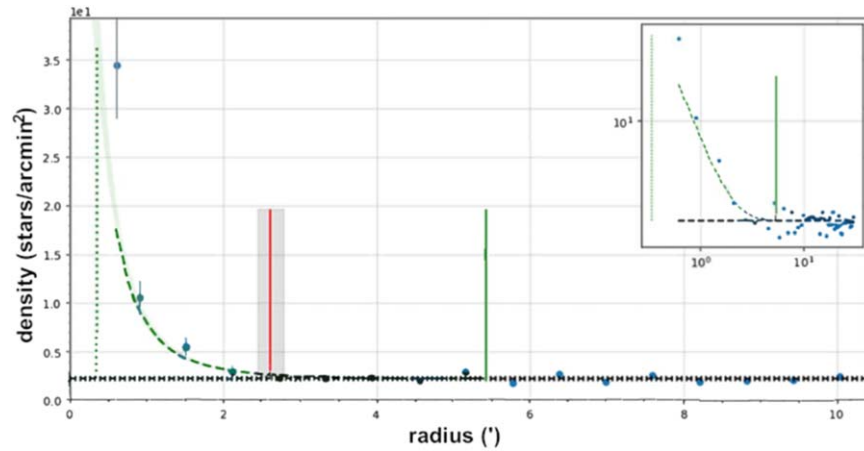


Figure 7. The combined BDBS photometry with radial density profile of the BH 261 cluster region determined using Gaia proper motions. The dots show the number of stars per arcmin² taking the cluster center as the origin. The horizontal dashed black line indicates the field density. The King profile fit is indicated with the green dashed curve and the cluster core radius is indicated by the dotted vertical green line. The red vertical line indicates the assigned radius of BH 261 with the uncertainty region shaded gray. The tidal radius is indicated by the solid vertical line at radius of 5.38. A rescale of the main plot is shown in the inset.

It is estimated that the contamination rate in the BDBS red clump star catalog is $\sim 30\%$ (30% of the stars are actually not red clump stars, instead belonging to, e.g., the bulge red giant branch, inner disk or halo; Johnson et al. 2022). Photometric metallicities may not be correct unless the star is in the red clump. In an attempt to remove any non-red-clump members contaminating our sample as well as to confirm the $[\text{Fe}/\text{H}]$ metallicities of the red clump stars, SP_ACE is run on the red clump stellar spectra with both photometric metallicities and radial velocities consistent with BH 261, i.e., those stars with radial velocities in the range $-35 > \text{RV} > -80 \text{ km s}^{-1}$ and a photometric $[\text{Fe}/\text{H}] < -0.5$. These are the most probable extra-tidal stars. Figure 8 (right panel) shows a comparison between the photometric and spectroscopic $[\text{Fe}/\text{H}]$ metallicities for the 16 red clump stars for which SP_ACE converged and that have parameters indicating they could be extra-tidal stars. Two of those have SP_ACE metallicities that are too metal-rich to be part of the cluster, and these are excluded from the sample of potential candidate extra-tidal stars.

The Gala Python package (Price-Whelan 2017; Price-Whelan et al. 2022) is used to generate a model of the dynamics of BH 261’s potential extra-tidal members. Gala provides several routines that allow the creation of mock stellar streams, by initializing new star particles at the cluster’s Lagrange points with a specified frequency and with randomized velocity offsets consistent with a specified velocity dispersion. The orbits of each set of new star particles are then evolved forward in time within the combined gravitational potential of the cluster plus the potential of the Galaxy to reveal the spatial and kinematic structure that would be expected at the present day. Using the cluster’s position (R.A. = $273^{\circ}.527$, decl. $-28^{\circ}.635$), distance (7.1 kpc), proper motion ($\mu_{\alpha} = 3.566 \text{ mas yr}^{-1}$, $\mu_{\delta} = -3.590 \text{ mas yr}^{-1}$), radial velocity (-61 km s^{-1}), and mass ($2.4 \times 10^4 M_{\odot}$), Gala calculates the cluster’s orbit in a Galactic potential. Here the adopted potential for the Milky Way is a three-component potential model consisting of the bar (an implementation of the model used in Long & Murali 1992), a Miyamoto–Nagai potential for the Galactic disk (Miyamoto & Nagai 1975), and a spherical Navarro–Frenk–White (NFW, Navarro et al. 1997) potential for the dark matter distribution. The bar is tilted with respect to the x -axis by 25° and has a mass 1/6 of the mass of the disk

component, and its long-axis scale length is set to 4 kpc (Bland-Hawthorn & Gerhard 2016).

We simulate the ejection of star particles using the Fardal Stream Generator (Fardal et al. 2015). The Fardal Stream Generator simulates the formation of extra-tidal structures via external tidal stripping, rather than more violent internal relaxation processes. The locations of the Lagrange points from which stars are ejected, as well as the velocity offsets the stars receive when they are ejected, are set to be consistent with the cluster’s mass and density profile and the velocity dispersion expected for a fully thermalized population. The frequency with which star particles are ejected, however, is nonphysical: we simulate ejection events every 0.5 Myr over the past 100 Myr to ensure that we densely sample all positions and velocities for which tidally stripped stars would be present.

A comparison of the location of the candidate extra-tidal stars we have identified with the synthetic extra-tidal stars in the Gala simulations is shown in Figure 9 (left panel). Because the most recent stellar debris will be both physically closest to the cluster and the most kinematically coherent, we focus on the debris produced within the last 100 Myr, which is most amenable to detection in our spectroscopic observations. Also, the simulated debris produced within the last 100 Myr is the least affected by the adopted potential of the Milky Way.

The Gala simulation does suggest that stars ejected from BH 261 could appear as a stream, with arms on the leading and trailing ends of the orbital path of the cluster. Our observations are limited to the brightest stars, which, given the low luminosity of BH 261, would likely not have the spatial density to show a clear stream. Still, we may be able to detect tidal disruption, which could follow a coherent structure. No stellar tidal streams have been seen emanating from bulge GCs to date, although a low-luminosity stream ($M_V = -3.0 \pm 0.5$, similar to that found for the lowest-mass GCs), the Ophiuchus stream, has been detected near the MW bulge region, above the center of the Galaxy (Bernard et al. 2014). Its old ($\sim 12 \text{ Gyr}$) and relatively homogeneously metal-poor population and α -enhanced stars suggest that the progenitor would most likely be a globular cluster (e.g., Sesar et al. 2015). However, because of the short length and short orbital period of the stream, it should have been disrupted fairly recently, but no progenitor is visible. In an attempt to explain the Ophiuchus stream, models and

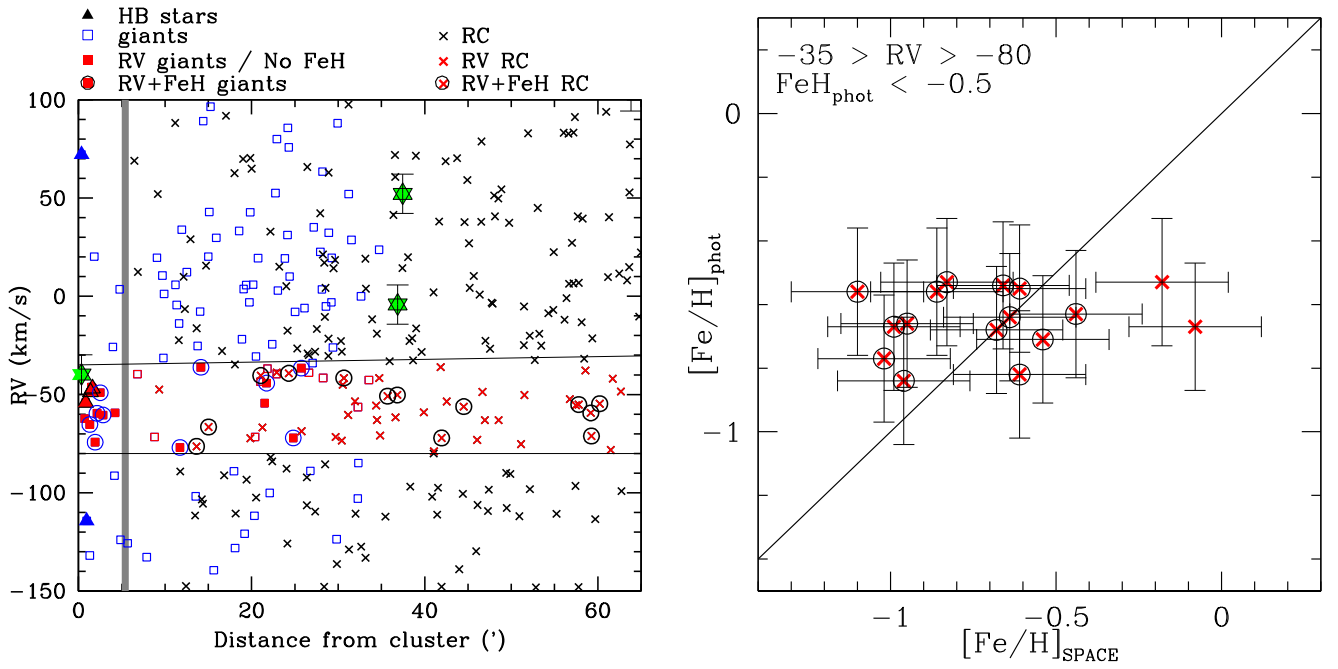


Figure 8. Left: the heliocentric velocities of our targeted stars within $65'$ of BH 261, with the tidal radius at $r_t = 5.4'$ indicated by the solid gray line. The uncertainty in radial velocity is $\sim 4 \text{ km s}^{-1}$, except for the horizontal branch stars, where the RV uncertainty is $\sim 9 \text{ km s}^{-1}$. Large (green) stars represent the targeted RR Lyrae stars. The stars with SP_ACE metallicities, photometric metallicities, and radial velocities consistent with BH 261 are circled, and are potential extra-tidal stars belonging to BH 261. Right: a comparison between the photometric $[Fe/H]$ and spectroscopic $[Fe/H]$ for the stars with both photometric metallicities and radial velocities consistent with BH 261. The two red clump stars with spectroscopic $[Fe/H]$ metallicities that are discrepant from the photometric ones also have T_{eff} and $\log g$ values that suggest they are not red clump giants.

mechanisms to enhance the density of some stellar streams in the inner halo/bulge have been put forward, but to date no model can explain the short Ophiuchus stream with such a short orbital period (e.g., Hattori et al. 2016; Price-Whelan et al. 2016; Lane et al. 2020). Observational analysis to detect additional substructures in the inner Galaxy is needed for a more complete understanding of the Milky Way’s gravitational potential and therefore a better dynamical study of clusters as they pass through the inner Galaxy, which is complicated also by the influence of the Galactic bar, its rotations, and how it has changed with time (e.g., Hattori et al. 2016).

Only a handful of the stars with radial velocities consistent with BH 261 are spatially coincident with the predicted 100 Myr tidal debris. Extra-tidal stars that do not fall along the cluster’s current orbit could have arisen due to effects not included in Gala, such as stars ejected due to shocks caused by the tidal field of the Galaxy and/or stars ejected from tidal interactions with the Galactic plane (e.g., Moreno et al. 2014), or a much larger dispersion of ejection velocities and angles due to intracluster interactions, such as those simulated by the core particle spray algorithm (Grondin et al. 2023). Although less significant, stars can also be ejected due to interactions with the giant molecular clouds (e.g., Amorisco et al. 2016), a process Gala is unable to incorporate.

Given the large velocity dispersion of BH 261 and hence a potentially larger dynamical mass, we also used Gala with a cluster mass more in line with the dynamical mass of the cluster, $1 \times 10^6 M_{\odot}$. Figure 9 (right panel) shows that in this case the comparison of the observed extra-tidal stars with simulations is improved.

High-resolution spectroscopy to chemically fingerprint the candidate extra-tidal stars would allow a deeper characterization of the origin of these stars. There are a handful of

candidate extra-tidal stars that fall along the predicted tidal debris, but it is likely that most of the candidate extra-tidal stars listed in Table 3 are not recently stripped from the cluster. That few stars are currently being stripped from BH 261 would be in agreement with the cluster’s low luminosity—the cluster does not have as many stars left for it to lose today as it had in the past. This would be consistent with BH 261 being an old, low-mass cluster so that any extra-tidal stars are likely to be white dwarfs, rather than more massive main-sequence stars and giants. In this case, it would be difficult to detect extra-tidal stars from our observations. If the extra-tidal candidates are confirmed to be bona fide extra-tidal stars, that might indicate the velocity dispersion of BH 261 is driven by tidal heating rather than a high mass-to-light ratio.

4. Conclusions

In order to better understand the bulge field population as well as to observe the processes that GCs undergo in their passage through the inner Galaxy, the MWBest spectroscopic survey is identifying stripped stars from inner Galaxy GCs. On average, mass lost from low-mass/low-luminosity GCs in the inner parts of the Milky Way, such as BH 261, will be considerably larger than for clusters with present-day masses larger than $10^5 M_{\odot}$ (Baumgardt & Vasiliev 2021). These low-mass/low-luminosity clusters started off with masses greater than $\sim 10^6 M_{\odot}$ and have lost mass as they move through the Galaxy. By integrating the orbits of the Milky Way GCs backward in time and applying suitable recipes to account for the effects of dynamical friction and mass loss from stars to the clusters, Baumgardt & Vasiliev (2021) show that clusters, especially those inside the central 2 kpc of the MW, have lost a large portion ($\sim 80\%$) of their initial populations. BH 261 has the smallest mass of the Milky Way GCs listed in Baumgardt &

Table 3
Positions, Gaia Proper Motions, Radial Velocities, and Spectroscopic [Fe/H] Metallicities of the Candidate Extra-tidal Stars Stripped from BH 261

Gaia ID (1)	R.A. (deg) (2)	Decl. (deg) (3)	μ_{α} (mas s ⁻¹) (4)	μ_{δ} (mas s ⁻¹) (5)	HRV (km s ⁻¹) (6)	[Fe/H] (7)	r (arcmin) (8)
Red clump stars							
4050678902240441728	273.47989	-28.41042	3.117 ± 0.060	-4.065 ± 0.040	-76.4 ± 3.2	-1.02	13.639
4050583038419373568	273.66186	-28.83802	3.754 ± 0.048	-5.041 ± 0.035	-66.5 ± 4.3	-0.96	15.034
4050609598466008576	273.86595	-28.64076	2.418 ± 0.065	-2.225 ± 0.048	-40.3 ± 1.9	-0.54	21.051
4050637704736314496	273.17874	-28.86039	2.854 ± 0.092	-4.043 ± 0.065	-39.2 ± 2.4	-0.64	24.289
4050611595682449152	274.02483	-28.67061	3.054 ± 0.043	-4.090 ± 0.032	-41.6 ± 2.0	-0.44	30.664
4050859531382762880	273.02371	-28.29882	4.076 ± 0.090	-2.628 ± 0.068	-50.8 ± 4.6	-1.10	35.719
4049822966614101376	273.83060	-29.16159	3.827 ± 0.068	-3.117 ± 0.049	-50.2 ± 3.3	-0.61	36.834
4050863826171182336	272.95921	-28.21074	3.688 ± 0.051	-2.835 ± 0.037	-72.2 ± 2.0	-0.66	41.954
4052192933885824896	274.04220	-28.11325	3.578 ± 0.048	-3.272 ± 0.039	-56.2 ± 1.7	-0.61	44.505
4050770986475829120	272.56501	-28.47638	4.074 ± 0.097	-4.250 ± 0.069	-55.1 ± 1.8	-0.99	57.790
4049707659748737920	273.46234	-29.62002	3.072 ± 0.059	-4.050 ± 0.041	-59.4 ± 1.8	-0.83	59.186
4052214473131206400	273.95238	-27.74946	3.838 ± 0.041	-3.343 ± 0.030	-71.1 ± 1.9	-0.68	59.260
4052143142313784960	274.37092	-28.11093	3.090 ± 0.043	-3.096 ± 0.031	-54.7 ± 1.7	-0.86	60.216
Giant stars							
4050622105410855296	273.70971	-28.61684	2.749 ± 0.039	-3.637 ± 0.030	-77.0 ± 1.8	-0.98	11.731
4050619425373339008	273.74356	-28.69270	2.780 ± 0.029	-3.489 ± 0.020	-36.2 ± 1.7	-1.51	14.143
4050681857034868608	273.70796	-28.33282	3.180 ± 0.038	-5.003 ± 0.028	-54.4 ± 1.4	...	21.511
4050642828694691584	273.17722	-28.76563	2.515 ± 0.042	-3.843 ± 0.032	-44.2 ± 1.7	-0.55	21.728
4050698113539687680	273.51378	-28.22135	3.185 ± 0.085	-3.431 ± 0.063	-72.1 ± 2.2	-0.80	24.820
4050695703975916416	273.33456	-28.24572	4.126 ± 0.040	-2.934 ± 0.028	...36.6 ± 1.9	-0.62	25.746

(This table is available in machine-readable form.)

Vasiliev (2021), weighing in at $\sim(2.4 \pm 0.6) \times 10^4 M_{\odot}$. It is also one of the few low-luminosity bulge GCs, with an absolute magnitude of $M_V = -4.43$ mag. In fact, there are only two well-studied bulge GCs (those with more than 10 stars with radial velocity measurements) listed in the Baumgardt & Vasiliev (2021) catalog with $M_V > -6$, the other one being ESO_452-SC11 (see Koch et al. 2017; Simpson et al. 2017).

In order to carry out a search for extra-tidal stars around the BH 261, a better characterization of this GC is needed. Using BDBS photometry combined with Gaia astrometry, the radial density profile of the cluster region is decontaminated and fit with a King profile using AStCA. In this way we derive a core radius of BH 261 of $r_c = 0'.35$, a cluster radius of $r_{cl} = 2'.6$, and a tidal radius of $r_t = 5'.4$.

We carried out the largest spectroscopic analysis of stars within the tidal radius of BH 261. From the seven giant stars with the best radial velocities within $\sim 4'$ of the center of BH 261, a mean velocity of $\langle RV \rangle = -61 \pm 2.6$ km s⁻¹ with a radial velocity dispersion of $\langle \sigma \rangle = 6.1 \pm 1.9$ km s⁻¹ is found. When all 12 BH 261 stars within $\sim 4'$ of the center are considered a mean velocity of $\langle RV \rangle = -56 \pm 1.7$ km s⁻¹ with a radial velocity dispersion of $\langle \sigma \rangle = 7.0 \pm 1.9$ km s⁻¹ is found. This average velocity is consistent with that of Barbuy et al. (2021), who find $\langle RV \rangle = -57.9 \pm 4.3$ km s⁻¹. It differs from that of Baumgardt et al. (2019), who find $\langle RV \rangle = -29.4$ km s⁻¹, and it differs from that of Geisler et al. (2023), who find $\langle RV \rangle = -44.9 \pm 3.8$ km s⁻¹. However, the stars observed here encompass the velocity values reported in previous studies. For example, the three observed stars in Barbuy et al. (2021) span a large velocity range with velocities of -67.65 ± 3.65 km s⁻¹, -57.93 ± 4.28 km s⁻¹, and -29.57 ± 5.85 km s⁻¹. Similarly, the three stars observed in Geisler et al. (2023) have velocities of -52.5 ± 1.9 km s⁻¹, -42.33 ± 1.2 km s⁻¹, and -39.9 ± 2.3 km s⁻¹. What is consistent in all

spectroscopic studies of BH 261 to date is that the velocity spread is not insignificant. The larger sample of stars presented here allows for a more robust value for a mean velocity.

The SP_ACE code was utilized for the determination of [Fe/H] metallicities, and from spectra of five giants, an average [Fe/H] $\sim -1.1 \pm 0.11$ dex is found. By identifying an RR Lyrae star in BH 261, the distance to the cluster is found to be 7.1 ± 0.4 kpc. This, as well as direct spectroscopic measurements of [Fe/H] from five giant stars in BH 261, confirms that BH 261 is on the near side of the bulge. As discussed also in Gran et al. (2022), this shorter distance indicates that BH 261 has an abnormally low luminosity as compared to its stellar velocity dispersion. New BDBS photometry in the *ugrizY* passbands is presented of the central region of BH 261 and is used to check for consistency between the cluster parameters and the optical CMD of BH 261. The MIST isochrones with the cluster's distance and metallicity derived in this work (7.1 kpc and -1.1 dex) show good agreement with the BDBS CMDs and with an old cluster age, of ~ 13 Gyr. Such an age is similar to that of other bulge GCs with blue HBs (Kerber et al. 2018).

A search for candidate extra-tidal stars spanning the range of radial velocity and proper motion of BH 261 was carried out. A few of our most promising extra-tidal candidates—those with radial velocities, proper motions, and [Fe/H] metallicities consistent with BH 261—are consistent with Gala simulations of the dynamical evolution of the cluster using its present-day mass. But most are only consistent with recent tidal debris from BH 261 if a larger cluster mass is used. BH 261 is an old, low-mass cluster, and it may be that most stripped stars today are white dwarfs, rather than more massive giants we are able to target spectroscopically.

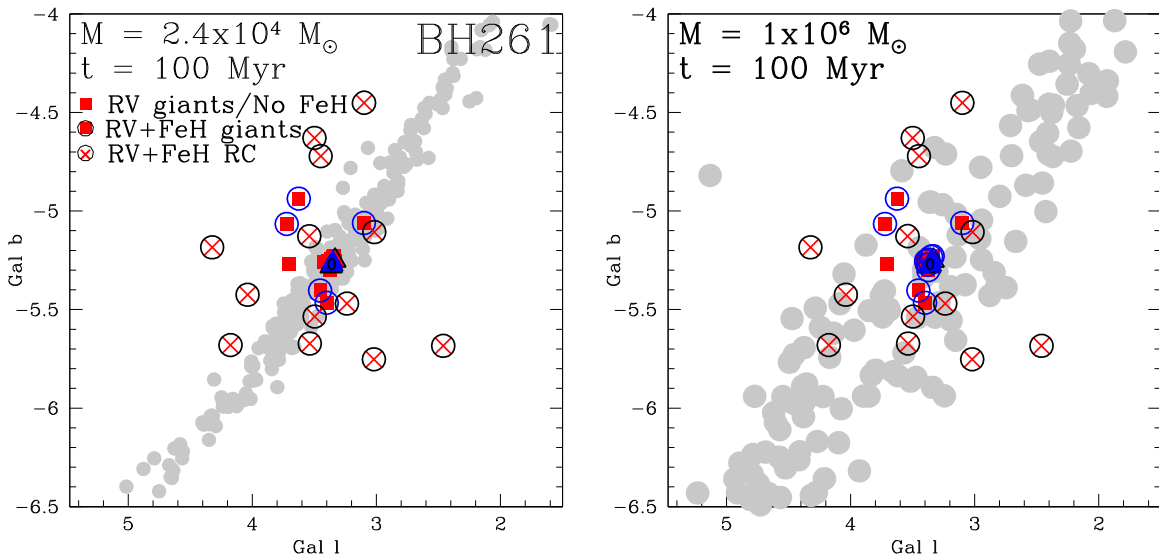


Figure 9. The simulated tidal tails for BH 261 (gray), calculated with the cluster’s best-fit parameters, are compared to the most promising BH 261 extra-tidal candidates presented here. The legend in the upper left corner indicates the length of time the cluster orbit is integrated forwards as well as the mass of BH 261 used in the simulation. The stream of the tidal debris has a narrow width when using a small GC mass (i.e., the mass inferred from its luminosity), and the simulated tidal tails occupy a greater area around the center of the cluster as a larger GC mass is used (i.e., the mass inferred from its velocity dispersion).

Acknowledgments

A.M.K. acknowledges support from grant AST-2009836 from the National Science Foundation. We gratefully acknowledge support from the M.J. Murdock Charitable Trust through its RAISE (Research Across Institutions for Scientific Empowerment) program, with matching funds from Saint Martin’s University. This work was made possible through the Preparing for Astrophysics with LSST Program, supported by the Heising-Simons Foundation and managed by Las Cumbres Observatory. M.J. gratefully acknowledges funding of MATISSE: *Measuring Ages Through Isochrones, Seismology, and Stellar Evolution*, awarded through the European Commission’s Widening Fellowship. This project has received funding from the European Union’s Horizon 2020 research and innovation program.

This project used data obtained with the Dark Energy Camera (DECam), which was constructed by the Dark Energy Survey (DES) collaboration. Funding for the DES Projects has been provided by the US Department of Energy, the US National Science Foundation, the Ministry of Science and Education of Spain, the Science and Technology Facilities Council of the United Kingdom, the Higher Education Funding Council for England, the National Center for Supercomputing Applications at the University of Illinois at Urbana-Champaign, the Kavli Institute for Cosmological Physics at the University of Chicago, Center for Cosmology and Astro-Particle Physics at the Ohio State University, the Mitchell Institute for Fundamental Physics and Astronomy at Texas A&M University, Financiadora de Estudos e Projetos, Fundação Carlos Chagas Filho de Amparo à Pesquisa do Estado do Rio de Janeiro, Conselho Nacional de Desenvolvimento Científico e Tecnológico and the Ministério da Ciência, Tecnologia e Inovação, the Deutsche Forschungsgemeinschaft and the Collaborating Institutions in the Dark Energy Survey.

The Collaborating Institutions are Argonne National Laboratory, the University of California at Santa Cruz, the University of Cambridge, Centro de Investigaciones Energéticas,












Medioambientales y Tecnológicas—Madrid, the University of Chicago, University College London, the DES-Brazil Consortium, the University of Edinburgh, the Eidgenössische Technische Hochschule (ETH) Zürich, Fermi National Accelerator Laboratory, the University of Illinois at Urbana-Champaign, the Institut de Ciències de l’Espai (IEEC/CSIC), the Institut de Física d’Altes Energies, Lawrence Berkeley National Laboratory, the Ludwig-Maximilians Universität München and the associated Excellence Cluster Universe, the University of Michigan, NSF’s NOIRLab, the University of Nottingham, the Ohio State University, the OzDES Membership Consortium, the University of Pennsylvania, the University of Portsmouth, SLAC National Accelerator Laboratory, Stanford University, the University of Sussex, and Texas A&M University.

Based on observations at Cerro Tololo Inter-American Observatory, NSF’s NOIRLab (NOIRLab Prop. ID 2013A-0529; 2014A-0480; PI: M. Rich), which is managed by the Association of Universities for Research in Astronomy (AURA) under a cooperative agreement with the National Science Foundation.

This work has made use of data from the European Space Agency (ESA) mission Gaia (<https://www.cosmos.esa.int/gaia>), processed by the Gaia Data Processing and Analysis Consortium (DPAC, <https://www.cosmos.esa.int/web/gaia/dpac/consortium>). Funding for the DPAC has been provided by national institutions, in particular the institutions participating in the Gaia Multilateral Agreement.

ORCID iDs

Andrea Kunder <https://orcid.org/0000-0002-2808-1370>
 Zdenek Prudil <https://orcid.org/0000-0001-5497-5805>
 Kevin R. Covey <https://orcid.org/0000-0001-6914-7797>
 Joanne Hughes <https://orcid.org/0000-0002-9074-0306>
 Meridith Joyce <https://orcid.org/0000-0002-8717-127X>
 Iulia T. Simion <https://orcid.org/0000-0001-8889-0762>
 Carlos Campos <https://orcid.org/0009-0009-4825-429X>

Christian I. Johnson  <https://orcid.org/0000-0002-8878-3315>
 Catherine A. Pilachowski  <https://orcid.org/0000-0002-3007-206X>
 Andreas J. Koch-Hansen  <https://orcid.org/0000-0002-9859-4956>
 Michael R. Rich  <https://orcid.org/0000-0003-0427-8387>
 Evan Butler  <https://orcid.org/0000-0002-1533-6004>
 William I. Clarkson  <https://orcid.org/0000-0002-2577-8885>
 Michael Rivet  <https://orcid.org/0009-0008-9816-4498>
 Kathryn Devine  <https://orcid.org/0000-0002-3723-6362>
 A. Katherina Vivas  <https://orcid.org/0000-0003-4341-6172>
 Gabriel I. Perren  <https://orcid.org/0000-0002-1852-9653>
 Mario Soto  <https://orcid.org/0000-0001-8444-9742>

References

- AAO Software Team, 2015 2dfdr: Data Reduction Software, Astrophysics Source Code Library, ascl:1505.015
- Amorisco, N. C., Gómez, F. A., Vegetti, S., & White, S. D. M. 2016, *MNRAS*, **463**, 21
- Andrews, A. D., & Lindsay, E. M. 1967, *IrAJ*, **8**, 126
- Barbuy, B., Ermandes, H., Souza, S. O., et al. 2021, *A&A*, **648**, 16
- Baumgardt, H., & Hilker, M. 2018, *MNRAS*, **478**, 1520
- Baumgardt, H., Hilker, M., Sollima, A., & Bellini, A. 2019, *MNRAS*, **482**, 5138
- Baumgardt, H., & Makino, J. 2003, *MNRAS*, **340**, 227
- Baumgardt, H., & Vasiliev, E. 2021, *MNRAS*, **505**, 5957
- Bensby, T., Yee, J. C., Feltzing, S., et al. 2013, *A&A*, **549**, 147
- Bernard, E. J., Ferguson, A. M. N., Schlafly, E. F., et al. 2014, *MNRAS*, **443**, L84
- Bland-Hawthorn, J., & Gerhard, O. 2016, *ARA&A*, **54**, 529
- Boeche, C., & Grebel, E. K. 2016, *A&A*, **587**, A2
- Boeche, C., Vallenari, A., & Lucatello, S. 2021, *A&A*, **645**, 35
- Carraro, G., Janes, K. A., & Eastman, J. D. 2005, *MNRAS*, **364**, 179
- Chadid, M., Sneden, C., & Preston, G. W. 2017, *ApJ*, **835**, 187
- Choi, J., Dotter, A., Conroy, C., et al. 2016, *ApJ*, **823**, 102
- Cohen, R. E., Mauro, F., Alonso-García, J., et al. 2018, *AJ*, **156**, 41
- Crestani, J., Fabrizio, M., Braga, V. F., et al. 2021, *ApJ*, **908**, 20
- Dékány, I., Grebel, E. K., & Pojmański, G. 2021, *ApJ*, **920**, 33
- Dias, B., Barbuy, B., Saviane, I., et al. 2016, *A&A*, **590**, 9
- Dias, B., Palma, T., Minniti, D., et al. 2022, *A&A*, **657**, A7
- Eisenstein, D. J., Weinberg, D. H., Agol, E., et al. 2011, *AJ*, **142**, 72
- Fardal, M. A., Huang, S., & Weinberg, M. D. 2015, *MNRAS*, **452**, 301
- Fernández-Trincado, J. G., Beers, T. C., Minniti, D., et al. 2021, *A&A*, **647**, 64
- Ferraro, F. R., Pallaanca, C., Lanzoni, B., et al. 2021, *NatAs*, **5**, 311
- For, B.-Q., Sneden, C., & Preston, G. W. 2011, *ApJS*, **197**, 29
- Gaia Collaboration, Brown, A. G. A., Vallenari, A., et al. 2021, *A&A*, **649**, A1
- Gaia Collaboration, Prusti, T., de Bruijne, J. H. J., et al. 2016, *A&A*, **595**, A1
- Gaia Collaboration, Vallenari, A., Brown, A. G. A., et al. 2023, *A&A*, **674**, A1
- Geisler, D., Parisi, M. C., Dias, B., et al. 2023, *A&A*, **669**, 115
- Geisler, D., Villanova, S., O'Connell, J. E., et al. 2021, *A&A*, **652**, 157
- Gnedin, O. Y., & Ostriker, J. P. 1997, *ApJ*, **474**, 223
- Gran, F., Zoccali, M., Saviane, I., et al. 2022, *MNRAS*, **509**, 4962
- Green, G. M., Schlafly, E. F., Finkbeiner, D., et al. 2018, *MNRAS*, **478**, 651
- Grondin, S. M., Webb, J. J., Leigh, N. W. C., Speagle, J. S., & Khalifeh, R. J. 2023, *MNRAS*, **518**, 4249
- Harris, W. E. 1996, *AJ*, **112**, 1487
- Hattori, K., Erkal, D., & Sanders, J. L. 2016, *MNRAS*, **460**, 497
- Johnson, C. I., Rich, R. M., Simion, I. T., et al. 2022, *MNRAS*, **515**, 1469
- Johnson, C. I., Rich, R. M., Young, M. D., et al. 2020, *MNRAS*, **499**, 2357
- Joyce, M., Johnson, C. I., Marchetti, T., et al. 2023, *ApJ*, **946**, 28
- Kader, J., Pilachowski, C., Johnson, C. I., et al. 2023, *ApJ*, **950**, 126
- Kerber, L. O., Nardiello, D., Ortolani, S., et al. 2018, *ApJ*, **853**, 15
- King, I. 1962, *AJ*, **67**, 471
- King, I. 1966, *AJ*, **71**, 276
- Koch, A., Grebel, E. K., & Martell, S. 2019, *A&A*, **625**, 75
- Koch, A., Hansen, C. J., & Kunder, A. 2017, *A&A*, **604**, 41
- Kunder, A., Bono, G., Pfill, T., et al. 2014, *A&A*, **572**, 30
- Kunder, A., Crabb, R. E., Debattista, V. P., Koch-Hansen, A. J., & Huhmann, B. M. 2021, *AJ*, **162**, 86
- Kunder, A., Kordopatis, G., Steinmetz, M., et al. 2017, *AJ*, **153**, 75
- Kunder, A., Mills, A., Edgecomb, J., et al. 2018, *AJ*, **155**, 171
- Kunder, A., Stetson, P. B., Cassisi, S., et al. 2013, *AJ*, **146**, 119
- Kundu, R., Fernández-Trincado, J. G., Minniti, D., et al. 2019, *MNRAS*, **489**, 4565
- Lane, J. M. M., Navarro, J. F., Fattahi, A., Oman, K. A., & Bovy, J. 2020, *MNRAS*, **492**, 4164
- Lauberts, A. 1982, ESO/Uppsala Survey of ESO(B) Atlas (Garching: ESO)
- Lee, Y.-W., Demarque, P., & Zinn, R. 1994, *ApJ*, **423**, 248
- Leon, S., Meylan, G., & Combes, F. 2000, *A&A*, **359**, 907
- Lim, D., Lee, Y.-W., Koch, A., et al. 2021, *ApJ*, **907**, 47
- Long, K., & Murali, C. 1992, *ApJ*, **397**, 44
- Marchetti, T., Johnson, C. I., Joyce, M., et al. 2022, *A&A*, **664**, 124
- Marín-Franch, A., Aparicio, A., Piotto, G., et al. 2009, *ApJ*, **694**, 1498
- Martell, S. L., Smolinski, J. P., Beers, T. C., & Grebel, E. K. 2011, *A&A*, **534**, 136
- Massari, D., Koppelman, H. H., & Helmi, A. 2019, *A&A*, **630**, 4
- Minniti, D., Fernández-Trincado, J. G., & Ripepi, V. 2018, *ApJ*, **869**, 10
- Minniti, D., Lucas, P. W., Emerson, J. P., et al. 2010, *NewA*, **15**, 433
- Miyamoto, M., & Nagai, R. 1975, *PASJ*, **27**, 533
- Moreno, E., Pichardo, B., & Velázquez, H. 2014, *ApJ*, **793**, 110
- Muñoz, C., Villanova, S., Geisler, D., et al. 2017, *A&A*, **605**, 12
- Navarro, J. F., Frenk, C. S., & White, S. D. M. 1997, *ApJ*, **490**, 493
- Nidever, D. L., Holtzman, J. A., Allende Prieto, C., et al. 2015, *AJ*, **150**, 173
- Ortolani, S., Bica, E., & Barbuy, B. 2006, *ApJ*, **646**, L115
- Parisi, M. C., Gramajo, L. V., Geisler, D., et al. 2022, *A&A*, **662**, A75
- Perren, G. I., Vázquez, R. A., & Piatti, A. E. 2015, *A&A*, **576**, 6
- Price-Whelan, A., Sipőcz, B., Starkman, N., et al. 2022, 131 adm/gala: v1.5, Zenodo, doi:10.5281/zenodo.6325733
- Price-Whelan, A. M. 2017, *JOSS*, **2**, 388
- Price-Whelan, A. M., Sesar, B., Johnston, K. V., & Rix, H.-W. 2016, *ApJ*, **824**, 104
- Pritzl, B., Smith, H. A., Catelan, M., & Sweigart, A. V. 2000, *ApJ*, **530**, 41
- Pritzl, B., Smith, H. A., Catelan, M., & Sweigart, A. V. 2001, *AJ*, **122**, 2600
- Prudil, Z., Kunder, A., Dekany, I., & Koch-Hansen, A. J. 2023, arXiv:2310.19438
- Rich, R. M., Johnson, C. I., Young, M., et al. 2020, *MNRAS*, **499**, 2340
- Romero-Colmenares, M., Fernández-Trincado, J. G., Geisler, D., et al. 2021, *A&A*, **652**, 158
- Ruchti, G. R., Fulbright, J. P., Wyser, R. F. G., et al. 2010, *ApJL*, **721**, 92
- Saviane, I., Da Costa, G. S., Held, E. V., et al. 2012, *A&A*, **540**, 27
- Schiavon, R. P., Zamora, O., Carrera, R., et al. 2017, *MNRAS*, **465**, 501
- Schlafly, E. F., & Finkbeiner, D. P. 2011, *ApJ*, **737**, 103
- Sesar, B., Bovy, J., Bernard, E. J., et al. 2015, *ApJ*, **809**, 59
- Simion, I. T., Belokurov, V., Irwin, M., et al. 2017, *MNRAS*, **471**, 4323
- Simpson, J. D., De Silva, G., Martell, S. L., Navin, C. A., & Zucker, D. B. 2017, *MNRAS*, **472**, 2856
- Sneden, C., Preston, G. W., Chadid, M., & Adamów, M. 2017, *ApJ*, **848**, 68
- Steinmetz, M., Guillaume, G., McMillan, P. J., et al. 2020, *AJ*, **160**, 83
- Tody, D. 1986, *Proc. SPIE*, **627**, 733
- Tody, D. 1993, in ASP Conf. Ser. 52, Astronomical Data Analysis Software and Systems II, ed. R. J. Hanisch, R. J. V. Brissenden, & J. Barnes (San Francisco, CA: ASP), 173
- van den Bergh, S., & Hagen, G. L. 1975, *AJ*, **80**, 11
- Vasiliev, E., & Baumgardt, H. 2021, *MNRAS*, **505**, 5978
- Zoccali, M., Lecureur, A., Barbuy, B., et al. 2006, *A&A*, **457**, L1